JOURNAL OF GEOPHYSICAL RESEARCH, VOL. 100, NO. A9, PAGES 16,999–17,013, SEPTEMBER 1, 1995

Coronal mass ejection and stream interaction region characteristics and their potential geomagnetic effectiveness

G. M. Lindsay, C. T. Russell, and J. G. Luhmann

Institute of Geophysics and Planetary Physics, University of California, Los Angeles

Abstract. Previous studies have indicated that the largest geomagnetic storms are caused by extraordinary increases in the solar wind velocity and/or southward interplanetary magnetic field (IMF) produced by coronal mass ejections (CMEs) and their associated interplanetary shocks. However, much more frequent small to moderate increases in solar wind velocity and compressions in the IMF can be caused by either coronal mass ejections or fast/slow stream interactions. This study examines the relative statistics of the magnitudes of disturbances associated with the passage of both interplanetary coronal mass ejections and stream interaction regions, using an exceptionally continuous interplanetary database from the Pioneer Venus Orbiter at 0.7 AU throughout most of solar cycle 21 (1979-1988). It is found that both stream interactions and CMEs produce magnetic fields significantly larger than the nominal IMF. Increases in field magnitude that are up to 2 and 3 times higher than the ambient field are observed for stream interaction regions and CMEs, respectively. Both stream interactions and CMEs produce large positive and negative B_z components at 0.7 AU ($\sim$14 nT on average), but only CMEs produce B_z magnitudes greater than 35 nT. CMEs are often associated with sustained periods of positive or negative B_z, whereas stream interaction regions are more often associated with fluctuating B_z. CMEs tend to produce larger solar wind electric fields than stream interactions. Yet stream interactions tend to produce larger dynamic pressures than CMEs. *Dst* predictions based on the solar wind duskward electric field and dynamic pressure indicate that CMEs produce the largest geomagnetic disturbances while the low-speed portion of stream interaction regions are least geomagnetically effective. Both stream interaction regions and CMEs contribute to low and moderate levels of activity with relative importance determined by their solar-cycle-dependent occurrence rates.

Introduction

Geomagnetic activity is caused by the transfer of momentum and energy from the solar wind to the magnetosphere that occurs in response to southward interplanetary magnetic fields (IMFs) [*Fairfield and Cahill*, 1966]. When the IMF possesses a southward component in the GSM coordinate system [*Hirshberg and Colburn*, 1969], reconnection between oppositely directed IMF and magnetospheric fields occurs on the dayside magnetopause [*Dungey*, 1961; *Aubry and McPherron*, 1971]. High solar wind velocities enhance the interaction by increasing the flux of energy transported into the magnetosphere. Reconnection produces forces that transport magnetic flux into the polar caps. Erosion of flux from the dayside magnetopause causes the nose of the magnetopause to move earthward 1-2 R_E [*Aubry et al.*, 1970]. The transported flux builds up in the magnetotail, increasing magnetotail lobe size and producing a thinning of the current sheet. In response to the drag applied to the Earth's magnetic field by the solar wind, the current sheet also moves earthward. About 1 hour after the southward turning of the IMF, reconnection begins in the tail. If the IMF remains southward for several hours, the associated steady duskward convection electric field energizes the ring current, thereby producing a geomagnetic storm. When the IMF again turns northward and reconnection ceases, the ring current decays, and the magnetosphere returns to a quiet state [*Burton et al.*, 1975].

Two sources of solar wind conditions contributing to geomagnetic storm production because of their associated strong southward interplanetary magnetic fields, high solar wind velocities, and enhanced solar wind dynamic pressures are fast/slow stream interactions and coronal mass ejections (CMEs). The stream interaction region represents the region of compression associated with the collision between high- and low-speed solar wind streams. Compared to the surrounding ambient solar wind, the plasma in the interaction region has higher density and magnetic field strength. Twofold magnetic field compressions and dynamic pressures

Paper number 95JA00525.
0148-0227/95/95JA-00525$05.00

3-4 times higher than average can occur [e.g., *Gosling et al.*, 1978]. As a spacecraft passes through the interaction region from the low-speed flow to the high-speed flow, an increase in velocity and ion temperature and a decrease in ion density are observed. The peak in magnetic field strength occurs just prior to entering the ambient high-speed flow. The fast stream portion of a stream interaction region can have speeds 1.5-2.5 times greater than the average solar wind. Because the fast stream portion also exhibits fluctuating magnetic fields and has a high probability of enhanced southward IMF, enhanced values of the duskward component of the solar wind electric field are likely in this region. However, since the duration of enhanced southward IMF is usually ~1 hour or less, the amount of sustained reconnection that may occur in conjunction with stream interaction passage is limited.

At 1.0 AU, the average CME travels at nearly the average solar wind speed (~380 km/s). Only a few percent of CMEs have speeds 2-3 times greater [*Gosling et al.*, 1987]. Because the bodies of CMEs typically have densities comparable to ambient, the dynamic pressure associated with their passage is not unusually large. However, about 30% of CMEs have a flux-rope-like magnetic field structure [*Gosling et al.*, 1990] that results in southward IMFs for a considerable fraction of the time during CME passage. Since CMEs at 1.0 AU are on average ~0.25 AU in width, the southward magnetic fields can persist for many hours. Increases in dynamic pressure and magnetic field magnitude associated with CME passage also occur when fast CMEs drive interplanetary shocks. The sheath region between the shock and the CME, characterized by compressed plasma, possesses both enhanced densities and velocities and strong magnetic fields. Field line draping also occurs in the sheath region [*Gosling et al.*, 1987], resulting in significant out-of-the-ecliptic magnetic field components. The combination of increased velocity and sustained southward IMF, in both the sheath region and the CME itself, combine to make CME passage at 1.0 AU conducive to dayside merging and geomagnetic storm production.

The association of high-speed recurrent streams with geomagnetic activity has been known for many years [e.g., *Sheeley et al.*, 1976]. Using Bartels diagrams, *Sheeley et al.* [1976] found an agreement between the recurrence patterns of coronal holes, high-speed solar wind streams, and geomagnetic disturbances. These diagrams show a repeatable pattern of enhanced geomagnetic activity with ~27-day period (approximately equal to the period of solar rotation). In a follow-on study, *Sheeley and Harvey* [1981] examined the change in recurrent storm patterns with solar cycle. It was found that unlike the speed enhancements that diminish in strength with solar cycle (V_{max} ~ 600-700 km/s at solar maximum versus V_{max} ~ 700-800 km/s at solar minimum), the recurrent disturbances maintain their high level of intensity. This finding suggests that it is not the high-speed streams themselves that cause the recurrent activity, but the combination of velocity shear and current sheet inclination that determines the severity of the associated stream interaction disturbances [e.g., *Pizzo*, 1991]. At solar minimum, the speeds are higher, but the current sheet inclination is less steep than at solar maximum when the fast streams are slower. These effects may balance out to maintain, on average, the same interplanetary disturbance size for the associated stream interactions.

Coronal mass ejections have been widely associated with geomagnetic storms, particularly storms producing the largest values of geomagnetic indices (*Ap*, *Kp*, *Dst*) [*Burlaga et al.*, 1987; *Tsurutani et al.*, 1990; *Gosling et al.*, 1991; *Farrugia et al.*, 1993]. Using ISEE 3 data, *Gosling et al.* [1991] concluded that 93% of all major geomagnetic storms (as defined by $Kp_{max} \geq$ 8- and $Kp \geq$ 6- for at least three 3-hour intervals during a 24-hour period) occurring from 1978 to 1982 were caused by CMEs driving interplanetary shocks. Using *Dst* as the geomagnetic storm index, *Tsurutani et al.* [1990] examined the same ISEE 3 data set and came to the similar conclusion that the largest storms were associated with CME passage. In the Gosling et al. study, the major storms comprised only ~4% of the total number of geomagnetic storms occurring in the period studied. Large storms, ~8% of the total, were also found to be primarily caused by CMEs driving shocks. The remaining ~88% of the storms were generally not associated with either CMEs or shocks. Overall, only ~37% of the geomagnetic storms in their study could be attributed to CMEs.

In efforts to understand the response of the magnetosphere to interplanetary conditions regardless of their origin, several studies have derived relationships between interplanetary values of velocity (V), density (ρ), the north/south component of the IMF (B_z), or combinations of those parameters VB_z, ρV^2, V^2B_z, and $(\rho V^2)^{1/3}VB_z$, and geomagnetic activity indices [*Siscoe*, 1966; *Burton et al.*, 1975; *Murayama*, 1982]. Because the *Dst* index is proportional to the strength of the ring current, and therefore directly related to the energy transported into the inner magnetosphere, it is the most appropriate geomagnetic index to examine in order to understand the coupling between the solar wind and the magnetosphere during the occurrence of geomagnetic storms. *Burton et al.* [1975] derived an empirical relationship for the rate of change of the *Dst* index in terms of the dawn-dusk component of the solar wind electric field, $E_y = -V_{sw} \times B_z$, and the dynamic pressure, ρV^2. Their formulation assumes that *Dst* is a function of magnetopause currents, ring currents, and tail currents. The contribution to *Dst* due to the magnetopause currents is assumed proportional to $(\rho V^2)^{1/2}$ (a relationship previously established by *Siscoe et al.* [1968] and *Ogilvie et al.* [1968]). The assumed sources of change in the strength of the ring current are the amount of injection ($F(E)$ = d (E_y - 0.5)) and the rate of decay, which is proportional to the strength of the ring current. In their formula, $dDst_o/dt = F(E) - aDst_o$, where $F(E)$ is nonzero only for southward solar wind magnetic fields (the half-wave rectifier assumption) and a is an empirically derived constant representing the rate of ring current decay. $Dst_o = Dst - b(\rho V^2)^{1/2} + c$ is the strength of the ring current adjusted for the strength of the magnetopause currents. The constants b and c, also empirically derived, represent the response to dynamic pressure changes in the solar wind and the quiet day currents, respectively. Since Burton et al. achieved excellent agreement between values of this index predicted from interplanetary measurements and

actual values of *Dst*, we use their formula here for the assessment of the potential geomagnetic effectiveness of interplanetary conditions.

The implications of previous studies are that CMEs produce the greater enhancements of the solar wind parameters necessary for major geomagnetic storm production, whereas stream interactions typically produce storms of lesser magnitude. However, studies specifically addressing this paradigm by systematically examining the signatures of both CMEs and stream interactions in large interplanetary databases have not been conducted. The aim of the present study is to determine the relative potential geomagnetic effectiveness of CMEs and stream interactions during solar cycle 21, based on their effects on the interplanetary medium. This is done by examining the characteristics of the important solar wind variables (V, B_z, and ρ) associated with the passage of each type of structure, as seen in an exceptionally complete interplanetary data set from the Pioneer Venus Orbiter (PVO). Combinations of those parameters that are known to affect geomagnetic activity, ρV^2 (dynamic pressure) and E_y (duskward component of the solar wind electric field), are examined for each to determine which phenomenon is likely to produce the greatest magnetospheric impact. The predicted *Dst* resulting from these disturbances is also calculated. Statistics of the geomagnetically important properties are determined and analyzed for CME sheath, CME, and pre-stream and post-stream interface periods. It is finally demonstrated that the *Dst* formula of *Burton et al.* [1975], applied to data obtained by the PVO at 0.7 AU, quite accurately predicts the daily level of the geomagnetic disturbance that will occur at 1.0 AU, illustrating the potential for increasing the lead time for predictions with inner heliosphere interplanetary monitors.

Data Analysis

The data used in this study were obtained on the Pioneer Venus Orbiter (PVO) spacecraft from 1979 to 1988, approximately the duration of solar cycle 21. PVO was launched May 20, 1978, entered Venus orbit on December 4, 1978, and entered the deep Venus atmosphere in late 1992. The spacecraft, its mission, and its instrument complement are described by *Colin* [1980]. The primary instruments providing the interplanetary measurements were the magnetometer [*Russell et al.*, 1980] and the plasma analyzer [*Intriligator et al.*, 1980]. For our purpose, the averaged 10-min-resolution University of California, Los Angeles, magnetometer data and the full 9-min-resolution plasma data as derived by the Ames Research Center investigators (both archived at the National Space Science and Data Center) were used. The coordinate system of the data is the Venus Solar Orbital system (VSO), wherein x lies in the orbital plane and points toward the Sun, z is directed north from the Venus orbital plane, and y lies in the orbital plane pointing opposite the direction of orbital motion. The orbit of Venus is inclined $\sim 3^\circ$ from the solar equator in contrast to Earth's 7.3°. The relationship between the VSO system and the geocentric solar magnetospheric (GSM) system is as follows: x lies in the orbital plane (within 3° of the ecliptic plane) and points toward the Sun in both VSO and GSM; y points opposite the direction of planetary motion; however, in GSM, y is perpendicular to the dipole axis so that it points below and above the ecliptic plane as the dipole axis rotates about the Earth's spin axis, whereas in VSO, y always lies in the Venus orbital plane; in both GSM and VSO, z completes the right-handed system, but in VSO, z points northward and is always perpendicular to the orbital plane, whereas in GSM, z points in the same sense as the northern magnetic pole but is not necessarily perpendicular to the ecliptic. In the following statistical study, we directly compare properties in the two different coordinate systems, assuming that since 10 years of data are considered, the differing directions of their polar axes do not alter the basic distribution of B_z values. However, for any particular storm, the precise direction of the magnetic field in GSM coordinates will depend on the time of arrival of the field at the Earth.

Observations

Figures 1 and 2 show typical examples of a stream interaction region and a CME as seen in the PVO plasma and magnetometer data. The top three panels show ion temperature, density, and velocity. The next two panels show total magnetic field, B_t, and the north/south magnetic field component, B_z. Two of the bottom three panels display the related time series of VB_z and ρV^2, which are considered the primary parameters in the production of geomagnetic activity. To explicitly consider the implied geomagnetic effectiveness of this stream interaction region, *Dst* computed from the *Burton et al.* [1975] formula with measurements of B_z and ρ at 0.7 AU scaled to 1.0 AU (assuming a r^{-1} and r^{-2} scaling, respectively) is shown in the bottom panel. Each figure spans a 2-day interval.

The stream interaction region in Figure 1 was identified by a sudden increase in ion temperature and velocity accompanied by a decrease in ion density. The stream interface, defined as the thin region that separates slow, dense plasma from fast, rarefied plasma [*Gosling et al.*, 1978], occurs where the change in velocity is steepest (January 31, 1985, at 1230 UT). A solid vertical line marks the stream interface position. An enhancement in the total magnetic field, approximately centered on the discontinuous change in plasma properties, is also observed. Prior to the interface, the north-south field component, B_z, varies slowly between southward (<0) and northward (>0), reaching a maximum magnitude in the northward direction in the 3 hours before the interface. The observed values of B_z and velocity give solar wind electric fields (shown in the sixth panel) $\sim \pm 3$ mV/m for most of the time preceding the interface. After the interface, B_z rapidly varies between southward and northward. The velocity throughout the 24 hours following this interface is ~ 650 km/s. The behavior of VB_z after interface passage mimics that of B_z, varying between $\sim \pm 8$ mV/m for ~ 12 hours following interface passage then decreasing gradually during the following 12 hours. According to the work of *Russell et al.* [1974], E_y must exceed 2 mV/m at 1 AU (~ 3 mV/m scaled to 0.7 AU)

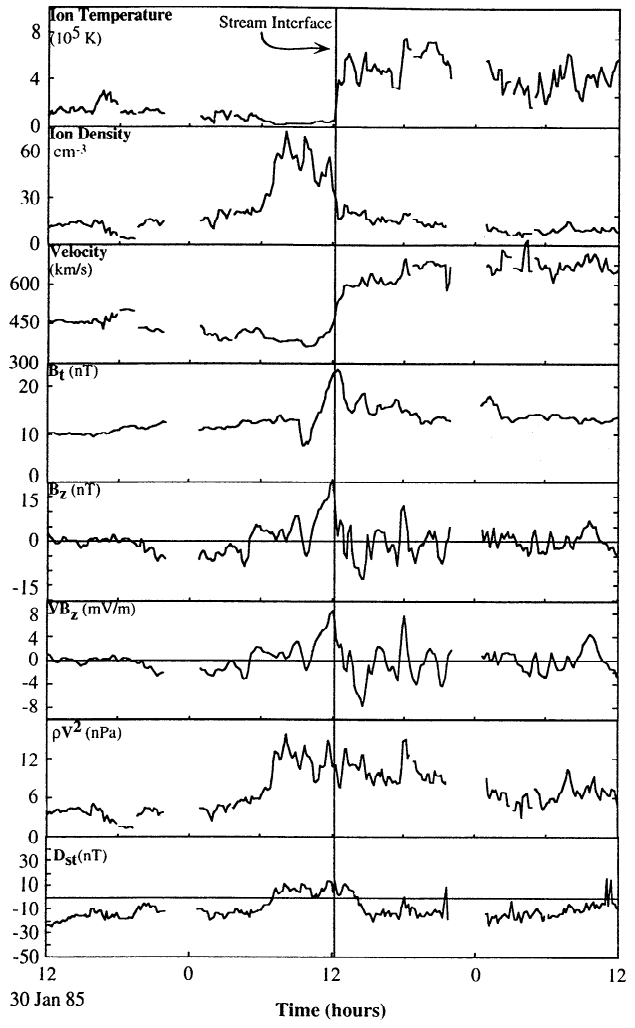

Figure 1. Typical example of a stream interaction as observed in the PVO data at 0.7 AU. Solid line notes time of stream interface passage.

in order to produce a geomagnetic storm. Here, the behavior of VB_z throughout the stream interaction region implies that the trailing portion of the stream interaction region will be more geomagnetically effective as it exhibits much larger values of duskward solar wind electric field with magnitudes greater than ~3 mV/m. Dynamic pressure, shown in the seventh panel, is ~3 nPa until ~5 hours prior to the stream interface, when the density increases suddenly. Even as the density begins to decrease toward the interface, dynamic pressure remains fairly constant for the following 12 hours because of the increase in velocity across the interface. In the trailing portion of the interface, dynamic pressure decreases slightly with the density, but is still higher than that preceding the interface.

The observed behavior of the solar wind electric field and dynamic pressure shown in Figure 1 can be used to explain the behavior of the predicted *Dst* seen in the bottom panel. First, during the interval preceding the interface where VB_z is small and negative, one would expect some reconnection to occur, with subsequent ring current energization. Dynamic pressure is at ambient values and relatively steady during this time, so the magnetopause currents are not enhanced. Thus the predicted values of *Dst* (shown in the eighth panel) are small in magnitude (~20 nT) and less than zero. Prior to the interface, VB_z becomes large and positive, and dynamic pressure suddenly increases. This behavior implies that reconnection will cease, the ring current will decay, and the magnetopause currents will become large. *Dst* will correspondingly become positive. After interface passage, the dynamic pressure remains elevated, and VB_z varies between positive and negative. Although the values of VB_z exceed the threshold magnitude of ~3 mV/m, VB_z is never less than zero long enough to generate a substantial ring current. So, while predicted *Dst* becomes negative, it remains at small magnitudes similar to the value prior to the interface (~20nT).

Figure 2 shows the corresponding example of a CME driving an interplanetary shock. The shock, marked by the dashed line, is identified by a discontinuous increase in ion temperature, density, velocity, and magnetic field magnitude. The sheath region, the interval between the shock and the CME boundary, is characterized by hot, dense, compressed plasma. In the sheath, the magnetic field is enhanced and

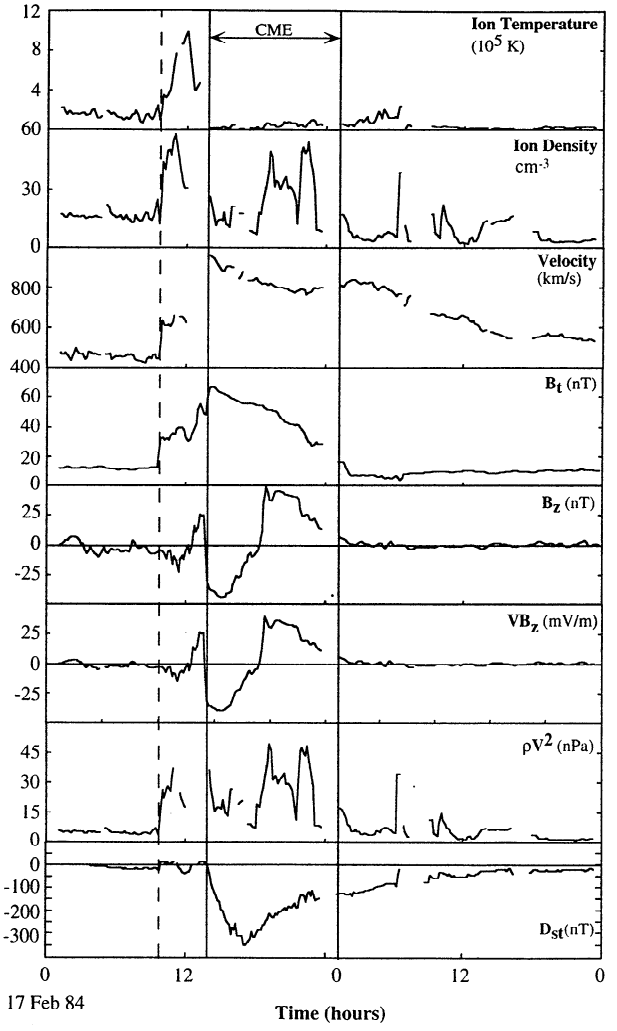

Figure 2. Typical example of a CME driving an interplanetary shock as observed in the PVO data at 0.7 AU. Dashed line marks interplanetary shock passage. Solid lines note CME start and end times.

rotates from southward to northward. The CME start time (February 17, 1984, 1455 UT) and end time (February 18, 1984, 021 UT) are noted by the solid lines. The defining characteristics of the CME are the below-ambient ion temperature, monotonically decreasing velocity, and smoothly varying total magnetic field. The smooth, large-scale rotation in B_z, from southward to northward, further suggests that this CME is a magnetic cloud [*Klein and Burlaga*, 1982]. Compared to the stream interaction region in Figure 2, the CME and CME sheath shown here exhibit much larger values of both positive and negative VB_z than those observed either before or after stream interface passage. Further, the amount of time at negative values within the CME (the duration of the most geomagnetically effective conditions) is much longer than in the above case following stream interface passage. Across the sheath region, the velocity increases from ~800 km/s at the shock to ~950 km/s near the CME leading edge. B_z changes from southward, with a maximum magnitude of ~23 nT, to northward, with a maximum magnitude of ~25 nT. E_y exceeds the magnitude threshold of ~3 mV/m at 0.7 AU throughout about half of the sheath region (~3 hours). Within the CME, B_z changes from ~-40 nT to ~40 nT through ~10 hours of the CME, maintaining negative values for about 5 hours. B_z then decreases gradually to a magnitude of ~8 nT at the end of the CME. During this time, the velocity decreases from ~950 km/s to ~800 km/s. The combination of high velocity and large negative B_z gives solar wind electric field values exceeding the threshold set by *Russell et al.* [1974] for a sustained period of ~6 hours. This example demonstrates that both the sheath region and CME have the potential to be particularly geomagnetically effective in that they both produce long periods of duskward E_y.

Predicted values of *Dst*, calculated as in Figure 1, are shown for the CME in the eighth panel of Figure 2. This case shows striking differences from the stream interaction region case. Prior to the shock, where the dynamic pressure is near ambient and the magnetic field is slightly negative, small, negative predicted *Dst* values are obtained. At the shock, the dynamic pressure increases suddenly, and VB_z tends toward larger negative values. At this point, it is expected that the magnetopause currents will become large and have the greatest influence on *Dst*. Predicted *Dst* first becomes positive (~12 nT in this case), then in the sheath region, dynamic pressure decreases slightly during an interval of negative VB_z so that *Dst* becomes negative. When VB_z turns positive, reconnection is expected to cease, and *Dst* becomes positive also. During the first ~6 hours of the CME, VB_z is very large and negative, and dynamic pressure decreases. With sustained negative VB_z and subsequent reconnection, the ring current is substantially energized, and *Dst* should become very large and negative. Since the time it takes the ring current to decay is proportional to its strength, even after VB_z becomes large and positive in the trailing portion of the CME, the predicted *Dst* takes nearly 36 hours to recover to quiet time values.

Of course, the examples shown in Figures 1 and 2 do not represent in detail all variations exhibited in the nearly 200 cases of stream interaction regions and CMEs identified in the PVO database. Although all stream interaction regions have basic plasma variations in common, including magnetic field, velocity, and temperature increases and density decreases across the interface, the relative magnitudes of the variations, the time over which the changes occur, and the characteristics of the variation in B_z between northward and southward differ from case to case. CMEs are generally very individual. Although the CMEs in the PVO database have been identified on the basis of a common requirement of low temperature, slowly varying magnetic field, and monotonically decreasing velocity, the variations observed in the behavior and magnitude of north/south magnetic field and density vary dramatically from case to case. In order to characterize the nature of the CMEs and stream interaction regions observed in the PVO inter-planetary data, and their implied potential geomagnetic effectiveness, distributions of V, B_z, ρ, and various combinations of these parameters have been calculated.

The distributions of V, B_z, ρ, VB_z, and ρV^2, extrapolated to 1.0 AU by scaling B_z by r^{-1}, ρ by r^{-2}, and assuming V does not change significantly between 0.7 AU and 1.0 AU, are shown in Figures 3-7. The intervals of data used are the 48 hours centered about the time of stream interface passage and the 9 hours prior to the CME leading edge plus the time within the entire CME. A 9-hour duration prior to the CME leading edge was chosen for analysis consistency between this study and that of *Gosling et al.* [1991], enabling a comparison between findings. Nine hours exceeds the entire CME sheath region shown in Figure 1, but it is close to the average 11-hour sheath duration for all CMEs driving interplanetary shocks identified in the PVO database. The data set consisted of 103 stream interaction regions and 75 CMEs (25 driving interplanetary shocks). The stream interaction region parameter distributions include ~16,000 data points, and the CME parameter distributions include ~15,000 data points. Since this analysis concerns the potential geomagnetic effectiveness of either a stream interaction region or CME on the ambient solar wind, complex regions that result from a CME-stream interface interaction or a fast CME overtaking a slow CME are not included here (discussion of these types of interactions and their geoeffectiveness can be found in the paper by *Burlaga et al.* [1987]). This filter is imposed by considering only those events that do not occur within the 48 hours preceding or following the passage of another stream interface or CME leading edge. About 10% of the total number of stream interaction regions and CMEs in the PVO database were excluded by this criterion.

The distribution of solar wind velocity associated with stream interaction regions and coronal mass ejections observed at 0.7 AU is plotted in Figure 3. This plot shows the percent occurrence, on a linear scale, versus velocity. For comparison purposes, the distribution of all solar wind data at 1.0 AU (given by *Gosling et al.* [1991]) is also shown. It is immediately obvious that the bulk of the distributions from the CMEs (thick line) and the stream interaction regions (thin line) are similar. The CMEs have a median velocity of ~364 km/s, and the stream interaction

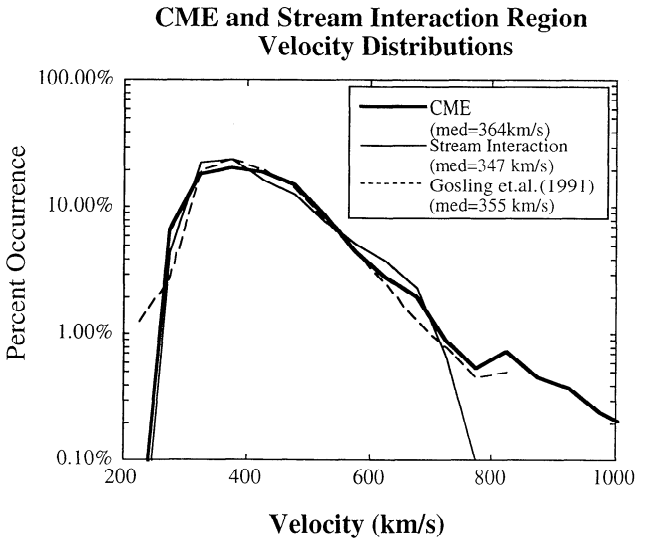

Figure 3. Comparison of the velocity distributions of solar wind at 1.0 AU (dashed line), CME at 0.7 AU (thick solid line), and stream interaction at 0.7 AU (thin solid line). Velocity is in 50-km/s bins.

regions have a median velocity of ~347 km/s. The differences in the two distributions arise in their high-velocity tails. The stream interaction region velocities extend to ~800 km/s, but the CME distribution exhibits a high-speed tail to velocities in excess of ~1000 km/s. The solar wind distribution has a median velocity of ~355 km/s, roughly equivalent to that of both the CMEs and stream interaction regions. The solar wind distribution ends at velocities ~100 km/s higher than the stream interaction region distribution and ~200 km/s less than the CME distribution.

The distribution of B_z magnitudes observed in association with the passage of CMEs and stream interaction regions at 0.7 AU, scaled to 1.0 AU, is shown in Figure 4, plotted in the same manner as Figure 3. The distribution of B_z for all solar wind data at 1.0 AU is also shown. As is expected, the medians of all three are ~0 nT, indicating that the field is as often northward (positive) as southward (negative). The stream interaction region distribution and the solar wind distribution have a similar range, ± ~24 nT. However, the CME distribution shows a large high-field tail for both positive and negative B_z. Both CMEs and stream interaction regions have median | B_z | of ~2.5 nT, whereas the solar wind has a median | B_z | of ~1.0 nT.

Figure 5 shows the related distribution of density. Percent occurrence is plotted on a linear scale versus density. This plot shows that both stream interaction regions and CMEs have characteristically higher densities associated with their passage than does the ambient solar wind. Further, stream interaction regions (median density = 8.2 cm^{-3}) tend to have higher associated densities than CMEs (median density = 7.3 cm^{-3}). This observation is a natural consequence of the fact that the solar wind is always compressed in a stream interaction region. On the other hand, the average CME travels near the solar wind speed and thus usually does not produce significant compression in the solar wind. Moreover, the bodies of CMEs typically have densities similar to the density of the surrounding solar wind. The enhanced densities in the CME density distribution result from a combination of the few fast CMEs compressing the ambient medium ahead and the few CMEs which are themselves denser than average.

From Figures 1 and 2, it is clear that the characteristics of V, ρ, and B_z change throughout the passage of a stream interaction region or a CME. The degree to which the solar wind associated with these phenomena becomes geomagnetically effective depends on the combination of these parameters and their duration. To determine which portion of the interplanetary disturbance associated with a CME or stream interaction region is most geomagnetically effective, the distributions of VB_z and ρV^2 have been separately computed for the 24 hours preceding (pre-stream interface) and following (post-stream interface) stream interface passage, and the 9 hours preceding the CME leading edge (pre-CME) and the time within the CME (post-CME). Pre-CME is used here instead of sheath region because both CMEs driving interplanetary shocks and those not driving interplanetary shocks were considered. These results are shown in Figures 6 and 7.

The distribution of the fundamental parameter in determining whether or not reconnection will occur, | VB_z | , is plotted in Figure 6. Here, the percent occurrence (plotted on a log scale) versus | VB_z | is shown with B_z scaled to 1.0 AU. The top panel displays the CME distributions; the bottom panel contains the stream interaction region distributions. Solid lines represent the pre-CME or pre-stream interface values, and dashed lines represent the post-CME or post-stream interface values. In both panels, the dashed line with the cross symbols represents the distribution

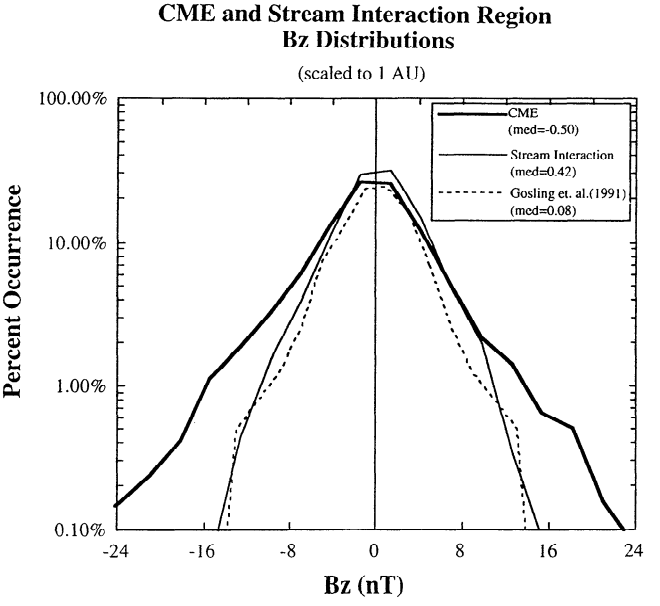

Figure 4. Comparison of total magnetic field distributions of solar wind at 1.0 AU (dashed line), CME at 0.7 AU (thick solid line), and stream interaction at 0.7 AU (thin solid line). CME and stream interaction fields scaled from 0.17 AU to 1.0 AU. Magnetic field is in 2-nT bins.

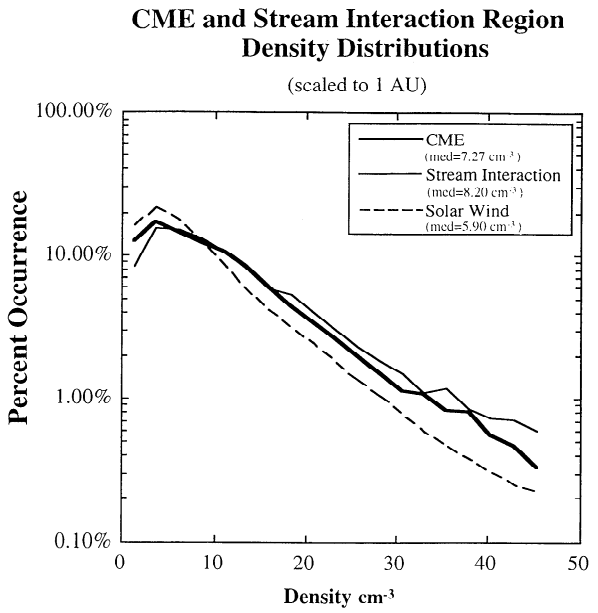

Figure 5. Comparison of the distribution of the ion density associated with solar wind at 1.0 AU (dashed line), CMEs at 0.7 AU (thick solid line), and stream interactions at 0.7 AU (thin solid line). Fields scaled from 0.7 AU to 1.0 AU. Density is in 5-cm^{-3} bins.

of the ambient solar wind data exclusive of the times associated with stream interaction regions or CMEs. It is notable that the pre-CME and post-CME distributions appear very similar. However, the pre-CME $| VB_z |$ median is ~0.58 mV/m, and the post-CME median is ~0.85 mV/m, ~51% larger than the pre-CME median. Considering the criterion that $| VB_z | > 2$ mV/m in order for a geomagnetic storm to occur, this figure indicates that approximately 29% of the pre-CME distribution and 24% of the post-CME distribution will produce geomagnetic storms. About 10% of both distributions are likely to produce major geomagnetic storms, according to the criterion of *Tsurutani et al.* [1990], who found that $| VB_z |$ values greater than ~5 mV/m are necessary for D_{st} < -100 nT. There is a greater difference between the distributions of pre-stream interface and post-stream interface periods, especially between 2 and 7 mV/m. The pre-stream interface median is ~0.36 mV/m. The post-stream interface median is ~0.56 mV/m, ~56% larger than the pre-stream interface median. Only ~13% of the pre-stream interface values and ~19% of the post-stream interface values exceed ~2 mV/m. Likewise, only ~1.5% of the pre-stream interface values and ~3.5% of the post-stream interface values are greater than ~5 mV/m. Figure 6 shows that both pre-CME regions and post-CME regions have characteristics more conducive to geomagnetic storms than either pre-stream interface or post-stream interface regions, especially for major storms. Further, conditions in the pre-CME regions seem slightly more favorable than conditions in the post-CME regions, but both regions are equally likely to produce major geomagnetic storms. On the other hand, the post-stream interface region appears slightly more favorable than the pre-stream interface region for geomagnetic storm production, although neither is very likely to cause major geomagnetic storms.

Figure 7 shows distributions of dynamic pressure in the same format as Figure 6. Percent occurrence is plotted on a log scale versus dynamic pressure in nanopascals. In the top panel the pre-CME and post-CME cases are very similar and demonstrate that equal magnitude dynamic pressures are likely to occur in both the pre-CME and post-CME regions. In contrast, in the bottom panel the pre-stream interface curve has a median of 6.5 nPa and extends beyond the cutoff of 20 nPa, whereas the post-stream interface curve has a range of 1 - 20 nPa and a median of 5.2 nPa. This demonstrates that higher dynamic pressures are more likely to occur in the pre-stream interface region. Although the velocity in the post-stream interface region is a factor of 2 greater than that in the pre-stream interface region, the density in the post-stream interface region is nearly an order

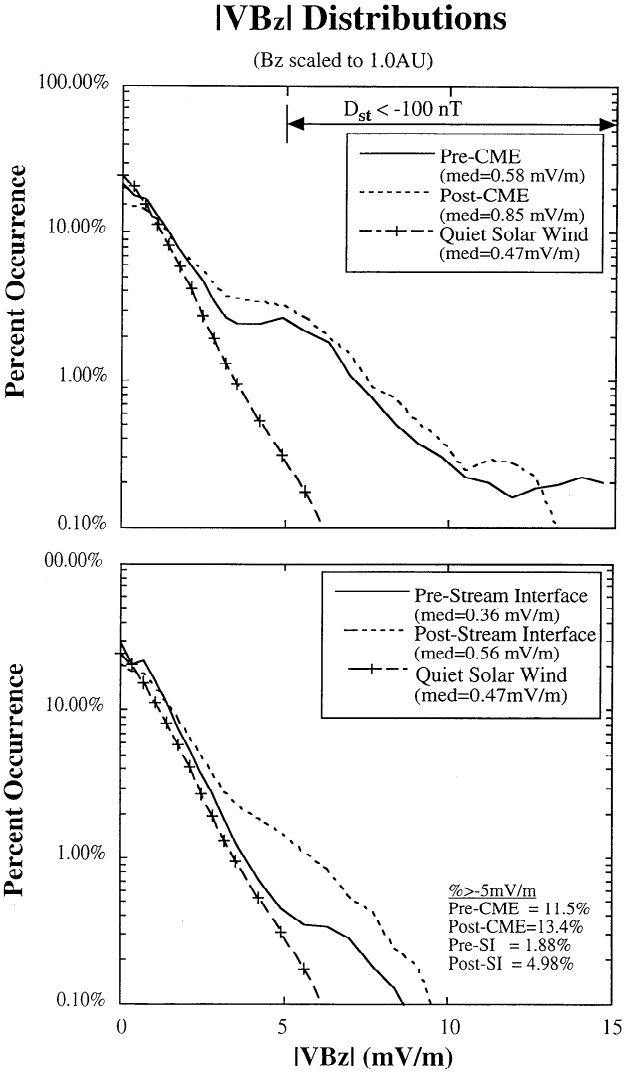

Figure 6. Comparison of the distribution of the duskward electric field magnitude produced prior to and after (top) CME and (bottom) stream interaction passage at 0.7 AU. Solar wind distribution at 0.7 AU (dashed line with cross symbol) included for comparison. Fields scaled from 0.7 AU to 1.0 AU. Electric field is in 0.5-mV/m bins.

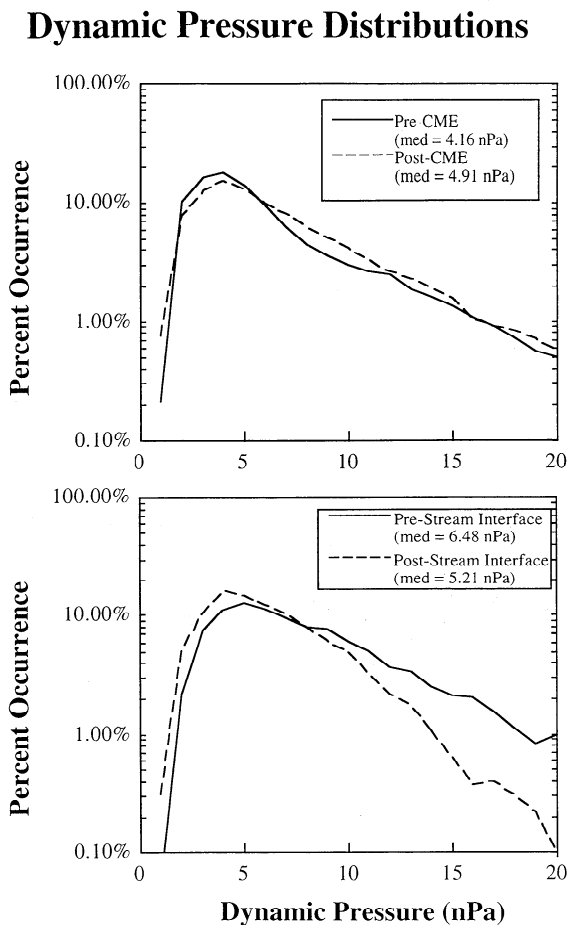

Figure 7. Comparison of the distribution of the dynamic pressure produced prior to and after (top) CME and (bottom) stream interaction passage at 0.7 AU. Solar wind distribution at 0.7 AU (dashed line with cross symbol) included for comparison. Fields scaled from 0.7 AU to 1.0 AU. Dynamic pressure is in 2-nPa bins.

of magnitude less than that in the pre-stream interface region. Thus dynamic pressure will generally be larger in the pre-stream interface region than the post-stream interface region. The median dynamic pressure for both the pre- and post-stream interface regions is higher than those of the pre- and post-CME regions. Increases in the horizontal component of the Earth's magnetic field (H) are related to the square root of the solar wind dynamic pressure [*Siscoe et al.*, 1968]. The observations shown in Figure 7 imply that the largest increases in H will result from CME passage, but more generally, an increase in H will result from stream interaction region passage. Further, the largest increases in H are likely to result from the passage of the pre-stream interface portion of the interaction region.

Although $B_z < 0$ is the key progenitor of geomagnetic storms, as mentioned above, the larger magnetic storms are associated with sustained geoeffective conditions. The characteristic temporal variations of VB_z associated with either stream interaction region or CME passage determine the time-integrated distributions of VB_z displayed in Figure 8. The time-integrated values are computed by summing the magnitude of VB_z at each data point multiplied by the duration of the time since the previous data point. The latter interval is usually 10 min, and the assumption is that VB_z does not vary significantly during this time. Only southward intervals of B_z are used for this calculation. The top panel shows that the influence of the pre-CME and post-CME regions are nearly the same (with medians of 68 and 69 Wb/m, respectively). The stream interaction region-associated distributions are quite different and show two distinct peaks. The pre-stream interface distribution is narrow and has a median of ~41 Wb/m; the post-stream interface distribution is broader and has a median of ~59 Wb/m. The major storm criterion of $| VB_z | > 5$ mV/m for at least 3 hours [*Tsurutani et al.*, 1992] implies an integrated minimum value of 54 Wb/m. Approximately 56% of both the pre-CME and post-CME distributions meet or exceed this level, which is expected, given that similarly large, sustained B_z and high velocity can occur in both regions. About 50%

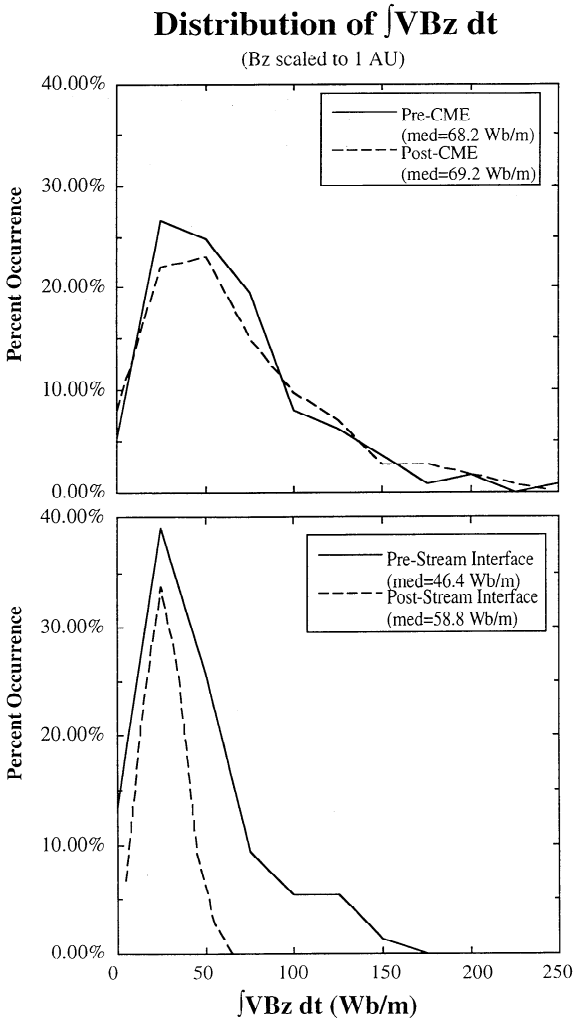

Figure 8. Comparison of the distribution of the time-integrated value of duskward electric field magnitude, in 25-Wb/m bins, produced prior to and after (top) CME and (bottom) stream interaction passage at 0.7 AU. Solar wind distribution at 0.7 AU (dashed line with cross symbol) included for comparison. Fields scaled from 0.7 AU to 1.0 AU.

of the post-stream interface distribution meets or exceeds this criterion, whereas only ~30% of the pre-stream interface distribution meets or exceeds this level. It has been shown that rapidly varying E_y is not as well rectified by the magnetosphere as steady E_y [*Burton et al.*, 1975]. Since E_y is relatively steady in the pre- and post-CME region and the pre-stream interface region compared to the post-stream interface region intervals, the percentage of post-stream interface regions actually producing major storms is likely to be less than the 50% indicated here.

Figure 9 shows the distributions of predicted *Dst*, calculated from the formula of *Burton et al.* [1975] for the CME and stream interaction region data scaled to 1.0 AU. Percent occurrence is plotted on a log scale versus *Dst* in nanoteslas. In the top panel, it is seen that the pre- and post-CME distributions peak at ~-10 nT. For *Dst* values greater than zero, both distributions are similar, ending at ~50 nT. For *Dst* values less than zero, the distributions are quite different. The post-CME distribution shows a greater likelihood of large negative values and, in fact, extends to ~-400 nT. The pre-CME distribution ends at ~-200 nT. These differences are reflected in the medians: ~-6.1 nT for the pre-CME distribution and ~-21.6 nT for the post-CME distribution. The pre- and post-stream interface distributions, shown in the bottom panel, are notably different from the CME distribution. The pre-stream interface distribution has a range of ~-100 nT to ~60 nT and a peak in the distribution at ~0 nT. The post-stream interface distribution has a range of ~-100 nT to 40 nT and peaks at ~-15 nT. Although the two distributions have similar ranges, the offset of the peaks is seen in the medians: ~-2.8 nT for the pre-stream interface distribution and ~-14.6 nT for the post-stream interface distribution. The distributions shown in Figure 9 suggest that both the post-CME and post-stream interface regions will produce larger geomagnetic storms than the corresponding pre-CME and pre-stream interface regions. According to the most likely *Dst* values, the order of decreasing geoeffectiveness is post-CME, post-stream interface, pre-CME, and pre-stream interface. This figure also indicates that ~3% and ~7% of the pre- and post-CME intervals and ~0.5% and ~2% of the pre- and post-stream interface regions, produced the most major storms with D_{st} < -100 nT during the period under study.

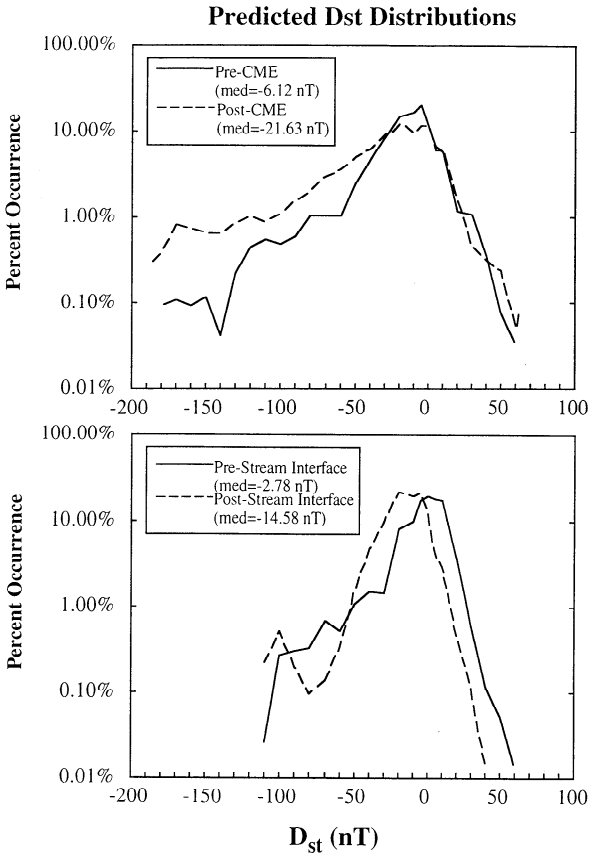

Figure 9. Comparison of the distribution of predicted *Dst* values produced prior to and after (top) CME and (bottom) stream interaction passage at 0.7 AU. Solar wind distribution at 0.7 AU (dashed line with cross symbol) included for comparison. Fields scaled from 0.7 AU to 1.0 AU. *Dst* is in 10-nT bins.

In general, the statistical distributions show that both CMEs and stream interaction regions produce solar wind conditions that are more conducive to geomagnetic storms than the normal solar wind. The greatest difference in solar wind conditions is found in the density characteristics of CMEs and stream interaction regions, both of which have higher median values than the normal solar wind. However, higher density in the absence of southward B_z acts only to increase the solar wind dynamic pressure and thus the strength of the magnetopause currents. Higher density alone does not produce a geomagnetic storm, so it does not distinguish the geomagnetic effectiveness of CMEs and stream interaction regions from that of the average solar wind. Rather, it is the portions of the distributions that additionally exhibit higher field and velocity enhancements which determine the geomagnetic potential of each phenomenon. The highest magnitudes in B_z and V are associated with CME passage. Although the total percentage of CMEs observed exhibiting extreme V, B_z, and ρ values is small, ~5%, this is approximately the percentage of CMEs (~4%) found by *Gosling et al.* [1991] to produce major geomagnetic storms. Thus the observation at 0.7 AU that ~5% of CMEs have markedly different characteristics than the normal solar wind or stream interaction regions is consistent with the 1-AU results.

The question of where in the disturbed regions conditions likely to produce geomagnetic storms exist is addressed in Figures 6 through 8. These figures show that the post-stream interface region is more likely than the pre-stream interface region to produce geomagnetic storms. In general, the maximum product of VB_z occurs just after the interface in the post-stream interface region, before the maximum velocity is reached, in agreement with the earlier study by *Sawyer and Haurwitz*, [1976], who found that stream interaction regions produced the maximum geomagnetic disturbances prior to the onset of the highest velocities. Similarly, Figures 6-8 suggest that statistically, the pre-CME and post-CME regions observed at 0.7 AU both have the same effect on the solar wind. This is similar to the observations at 1.0 AU indicating that conditions of

high geomagnetic effectiveness exist in both the pre-CME and post-CME regions [*Tsurutani et al.*, 1990; *Gosling et al.*, 1990].

Consideration of the duration of VB_z, as shown in Figure 8, elucidates how the velocity and B_z characteristics of CMEs and stream interaction regions together determine geomagnetic effectiveness. That the pre-CME and post-CME regions are nearly the same in this parameter shows that while the pre-CME region may have a varying sign of B_z, and therefore shorter durations of negative VB_z, the magnitudes of B_z in the compressed plasma of the sheath region are large. On the other hand, the post-CME region (the CME itself) may not contain particularly large field magnitudes, but B_z varies over long time scales. Thus large time-integrated values of VB_z are found in both regions associated with a CME, suggesting that each region is highly geomagnetically effective for all storm levels. In contrast, although B_z may remain either positive or negative for a long time in the slow flow ahead of a stream interface, the values of both B_z and VB_z in the region of slow flow are very small. In the fast flow behind the interface, the sign of B_z varies, so that the duration of $B_z < 0$ is not large. But the magnitudes of V and B_z are much larger than those in the slow flow ahead of the stream interface. For this reason, the time-integrated values of VB_z are smaller for the pre-stream interface region than the post-stream interface region. The fact that the pre-stream interface region has small sustained values of VB_z while the post-stream interface region has large but short-lived values of VB_z is what tends to make stream interaction regions generally less geomagnetically effective than CMEs. Nevertheless, as noted above, they can compete in the moderate storm categories.

Because of the combination of their associated dynamic pressure (Figure 7), VB_z (Figure 6), and duration characteristics (Figure 8), stream interaction regions have limited geomagnetic effectiveness (Figure 9). During passage of the pre-stream interface region, enhanced magnetopause currents, produced by enhanced solar wind dynamic pressures, and minimal reconnection occur. Thus during pre-stream interface region passage, *Dst* should generally increase, often becoming positive. During passage of the post-stream interface region, the magnetopause currents decrease, reconnection increases, and *Dst* decreases. However, in order to produce a $Dst < 0$ and a geomagnetic storm, there must exist enough reconnection to sufficiently energize the ring current to overcome the preexisting large magnetopause currents. Because large time-integrated values of VB_z do not often exist in the post-stream interface region, the amount of ring current energization is small, and *Dst* will most likely not become large and negative. This is seen in Figure 9, where the percentage of the post-stream interface region distribution that exhibits predicted $Dst < -100$ nT is $\sim 2\%$ compared to the value of $\sim 5\%$ implied in Figure 6. However, considering that $\sim 1.5\%$ of the major and large storms found by *Gosling et al.* [1991] could not be explained in terms of CMEs, stream interaction regions may provide the residual.

The effect of the combination of CME-associated dynamic pressure, VB_z, and duration characteristics given by the *Dst* index indicates the pre- and post-CME regions are not equally geomagnetically effective. This is contrary to observations at 1.0 AU based upon VB_z behavior indicating that conditions with equal geomagnetic potential exist in both the pre-CME and post-CME regions [*Tsurutani et al.*, 1990; *Gosling et al.*, 1990]. This difference most likely results from the fact that both studies based their conclusion on the interplanetary data during some of the largest geomagnetic storms. The largest storms are evidently associated with fast CMEs driving interplanetary shocks and the existence of large VB_z in both the sheath region and the CME. This study examines the characteristics of CMEs without regard to disturbance size, and shows that in general, not only is the pre-CME region less geomagnetically effective than the post-CME region, but it is also statistically less geomagnetically effective than the post-stream interface region. The magnitude of B_z in the CME is generally larger than that of the surrounding solar wind [*Gosling et al.*, 1990]. The magnitude of B_z in the CME sheath increases with increasing CME velocity due to compression and draping. Thus the conclusion can be made that as the CME velocity increases, the geoeffective potential of the pre- and post-CME regions becomes more similar.

Akasofu [1964] noted that storm commencements can occur without a subsequent main phase, and that main phases may occur without a preceding commencement phase. Examination of the dynamic pressure (Figure 7) and solar wind electric field characteristics (Figure 6) associated with stream interaction region and CME passage may provide an explanation of these observations. Stream interaction regions generally produce larger dynamic pressures, but CMEs generally produce larger, more sustained electric fields. Thus as a stream interaction region passes, an initial phase can occur due to the increase in dynamic pressure associated with the compression in the interaction region, but no main phase occurs because the fluctuating sign of B_z precludes efficient energy transfer to the magnetosphere. Likewise, a main phase with no preceding initial phase is possible owing to CME passage. As the CME passes 1.0 AU, dynamic pressure is not likely to vary much from ambient; thus no initial phase is produced. However, large, sustained southward magnetic fields are probable, producing sustained reconnection and efficient energy transfer from the solar wind to the magnetosphere. The ring current will be energized, and a recognizable main phase will occur.

As shown by *Lindsay et al.* [1994], the occurrence rates and strengths of the CMEs and stream interaction regions observed by the PVO exhibit a solar cycle variation. The effect of this variation on geoeffectiveness was studied by examining the distribution of the previously considered parameters during solar maximum (1979-1981), the declining phase (1982-1984), and solar minimum (1984-1987). In all three periods, this analysis gave nearly the same results as are shown in Figures 3-7. During all three phases of the solar cycle, CMEs exhibit the largest median values and highest-value distribution tails in all parameters. Also, the relative potential geomagnetic effectiveness of the pre- and post-stream interface regions and pre- and post-CME regions, as shown in Figures 8 and 9, was preserved

throughout the solar cycle. That is, the pre- and post-CME region distributions are very similar and are much more geomagnetically effective than the ambient solar wind. The stream interaction region distributions show that the post-stream interface region is more geomagnetically effective than the pre-stream interface region and that the pre-stream interface region effects are comparable to those of the ambient solar wind. Although the occurrence rates and strengths of CMEs and stream interaction regions change throughout the solar cycle, their relative potential geomagnetic effectiveness does not. This result for stream interaction regions is consistent with the previously mentioned observations of *Sheeley and Harvey* [1981], that the intensity of stream-related recurrent disturbances did not show a solar cycle variation.

Potential for Long-Lead Time Dst Predictions

It is instructive to consider the possibility of forecasting observed values of *Dst* at 1.0 AU from observations in the solar wind at 0.7 AU. Figures 10, 11, and 12 show the comparison of predicted and observed *Dst* for three time periods during 1979-1988 when the PVO spacecraft travels from $\sim 10^{o}$ eastward to $\sim 10^{o}$ westward of the Earth-Sun line. In each figure, the thin line shows *Dst* values predicted from 0.7 AU observations using the *Burton et al.* [1975] formula. The thick line represents the observed values of *Dst* obtained from midlatitude ground stations at 1.0 AU. The pertinent parameters for this calculation, solar wind electric field (mV/m) and dynamic pressure (nPa), are shown in the bottom two panels of Figures 10, 11, and 12. As before, it is assumed that solar wind velocity does not vary appreciably between 0.7 AU and 1.0 AU and that the values of ρ and B_z vary as r^{-2} and r^{-1}, respectively. For comparison purposes, 1-hour averages of the PVO predictions were computed, then a 48-hour running average was calculated for both data sets. Smoothing over 12, 24, 36, and 48 hours was tested. The 48-hour average result is shown here because it produced the best comparison between predicted and observed *Dst*. Smoothing at less than 48 hours leaves many small variations which do not clearly project from 0.7 AU to 1.0 AU. With this treatment, only the longer time scale variations in *Dst* are being compared, eliminating daily variations in *Dst* due to the change in the Earth's dipole axis with respect to the ecliptic plane.

No time lag representing the transit time from 0.7 AU to 1.0 AU has been applied to the 0.7-AU data shown here. As will be shown, this time varies in an expected manner according to the prevailing speed of the solar wind or disturbance features. When Venus and Earth are in near alignment, the time delay between observations of a CME at the two locations is just that determined by the velocity of the CME, which is presumed to travel radially outward. Stream interaction regions are corotational solar wind features, so that the time delay between observations at 0.7 AU and 1.0 AU will depend upon the east/west angle of separation between Venus and Earth. When Venus is eastward to just westward of the Earth-Sun line, PVO will observe the stream interaction region first. The stream interaction region will then be observed at Earth at a time determined by the angular separation between Earth and Venus and the corotational speed and archimedean spiral angle of the interaction region. As PVO travels from east to west of the Earth-Sun line, the time between observations at 0.7 AU and 1.0 AU will decrease. When PVO is $\sim 18^{o}$ west of the Earth-Sun line, the stream interaction region may be detected nearly simultaneously at 0.7 AU and 1.0 AU. Since the comparisons shown in Figures 10, 11, and 12 are for time periods when PVO is within 10^{o} of the Earth-Sun line, it is not expected that a simultaneous 0.7 AU/1.0 AU stream interaction region observation will be found.

Figure 10 shows predicted versus observed *Dst* values for June 1-30, 1980. During this time, the Venus orbital and ecliptic planes were practically coincident. The agreement in the variation and magnitude of predicted and observed *Dst* is quite good. The major difference in magnitude occurs during the period when $Dst < 0$ on June 5-10, 1980. PVO predicts a maximum negative *Dst* of ~ 30 nT while a maximum negative *Dst* of ~ 45 nT is observed. During this time, two stream interaction regions (on June 5 and 20, 1988) and two CMEs (on June 10 and 26, 1980) are observed at 0.7 AU. Both stream interaction regions are associated with predicted increases of *Dst* to near zero. However, the first stream interaction region produces a significant decrease in *Dst* whereas only a slight decrease in *Dst* occurs after passage of the second stream interaction region. This behavior is predicted as well as observed. In both cases, the maximum magnitude of positive *Dst* is underpredicted. The first stream interaction region appears to have been more conducive to reconnection (indicated by $Dst < 0$) due to more southward B_z. The second stream interaction region is more conducive to magnetospheric compression as suggested by the substantial period of $Dst > 0$ resulting from its higher dynamic pressures. Both CMEs are associated with predicted and observed periods of large, negative *Dst*. The CME observed during the first period has a peak velocity of ~ 600 km/s and southward B_z of ~ 20 nT. The second CME has a peak velocity of ~ 400 km/s and southward B_z of ~ 15 nT. The longer duration of negative *Dst* following the first CME probably occurred because B_z was southward for a longer period during the first CME than the second CME.

An examination of Figure 10 indicates that the time lag between the predicted and observed *Dst* curves varies during the 30-day period. For example, the increase in *Dst* between June 1 and 2, 1980, is observed at 1 AU ~ 50 hours later than at PVO, and the decrease in *Dst* occurring between June 7 and 9, 1980, is observed at 1 AU ~ 36 hours later. Likewise, the increase in *Dst* predicted from PVO data on June 14-17, 1980, is observed at 1 AU ~ 58 hours later. The decrease predicted between June 23 and 24, 1980, is observed at 1 AU ~ 40 hours later. This indicates that the stream interaction region characteristics that produced the observed increases in *Dst* were traveling at ~ 250 km/s and ~ 215 km/s. The inferred velocities are less than those observed, but the relative difference in timing and inferred velocity is consistent with the fact that the velocity of the low-speed portion of the first stream interaction region is

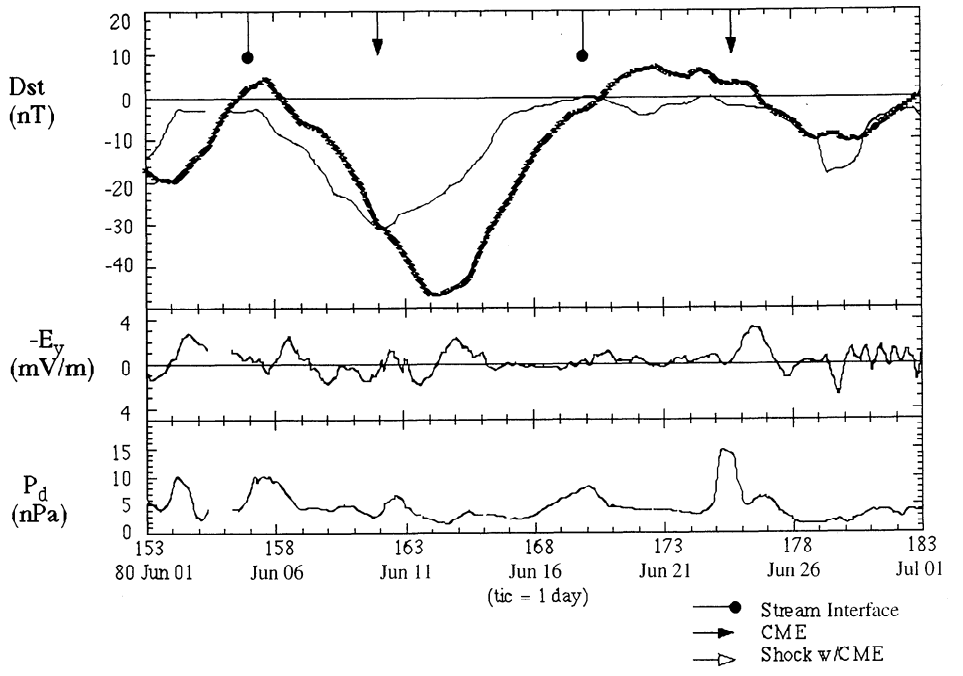

Figure 10. (Top) comparison of predicted *Dst* from PVO data (thin line) and observed *Dst* from midlatitude ground stations (thick line) during June 1980. (Middle) Solar wind electric field. (Bottom) Dynamic pressure.

higher than that of the second stream interaction region (~325 km/s versus ~300 km/s). The times associated with the CME conditions producing the predicted and observed decreases in *Dst* indicate that the solar wind was traveling at ~350 km/s and ~310 km/s. Although the relative magnitudes of the inferred speeds are consistent with observations, that is, they indicate that the first CME (~620 km/s) was moving faster than the second CME (~360 km/s), the inferred speeds are a factor of 2 slower than the observed speeds.

Excellent agreement between *Dst* predictions and observations during January 1982 is shown in Figure 11. Both the variations and magnitudes for *Dst* < 0 are well comparable. In this case, radial alignment occurs on January

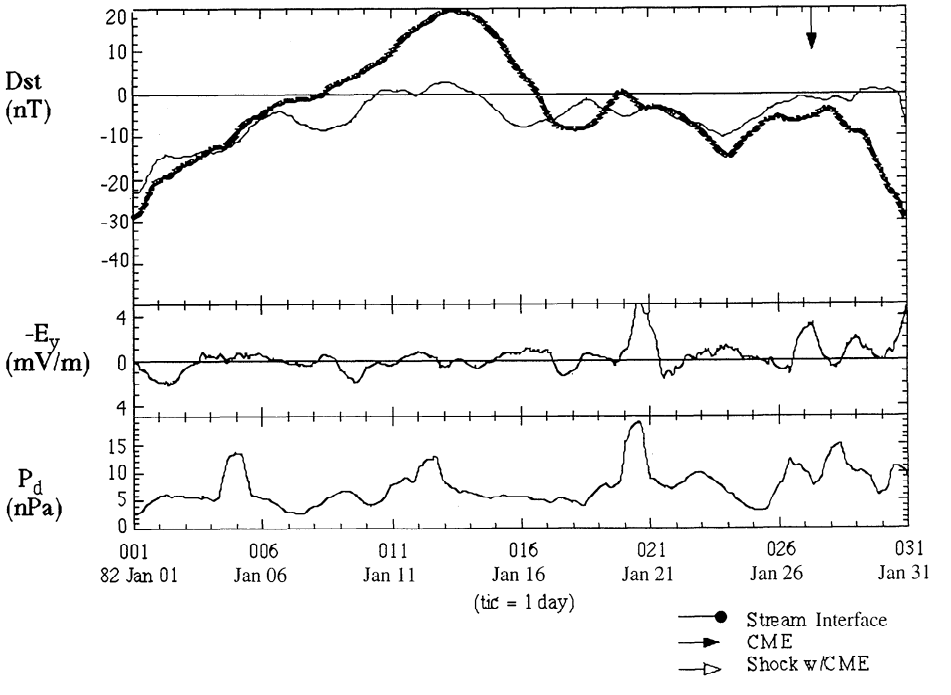

Figure 11. (Top) Comparison of predicted *Dst* from PVO data (thin line) and observed *Dst* from midlatitude ground stations (thick line) during January 1982. (Middle) Solar wind electric field. (Bottom) Dynamic pressure.

20, 1982, and Venus and Earth are never separated by more than 1° in the north-south direction. Examination by eye shows that the apparent time delay changes throughout the month: ~8 hours for January 1-7, ~45 hours for January 8-20, and ~24 hours for January 21-30. This trend in time delays is not consistent with the relative solar wind speeds observed during this time. The fastest solar wind speeds are observed during January 21-31, when the second longest time delay of 24 hours is inferred. However, the very fast inferred solar wind speeds of January 1-6 (1500 km/s) occurred during a time period of only slightly enhanced observed solar wind speeds (500 km/s). The apparent time delays during the rest of the month imply slower transit speeds than what is inferred from observation: 275 km/s implied, 375 km/s observed for January 7-20; 520 km/s implied, 550 km/s observed for January 21-31. Notably, the difference between the implied and observed speeds decreases as the alignment between Earth and Venus becomes more radial. There also seems to be a shift in time delay from ~45 hours to ~24 hours surrounding the time of nearly radial alignment. This trend is consistent with the observed velocity shift in this time period from 400 km/s to 550 km/s. The interplanetary disturbances observed during this interval are the CMEs on January 27 and 30. The CME on January 27, 1982, produces a small increase followed by a decrease in predicted and observed *Dst*, whereas the CME on January 30, 1982, produces a more dramatic decrease in predicted and observed *Dst* to values less than ~-50 nT. This difference probably occurs because the second CME has much larger velocities (~600 km/s versus ~500 km/s) and larger, more sustained southward B_z.

Figure 12 shows predicted *Dst* and observed *Dst* during March 16 through April 15, 1985. This case has the largest north/south separation as Venus moves from ~4° north to ~1° north of the Earth's ecliptic plane during this period. Near radial alignment occurs around April 2, 1985. Although the observed levels of activity are well predicted, predictions varying between ~±10 nT and observations varying from ~2 nT to ~-20 nT, the day-to-day variations are not as well predicted as in the previous cases. Here the solar wind is fairly steady, and most fluctuations are small. The one exception occurs between March 30 and April 7 near radial alignment. During this period, a fast/slow stream interaction region is observed at 0.7 AU. Like the second stream interaction region shown in Figure 10, passage of this stream interaction region is characterized by an increase of predicted *Dst* to positive values followed by a slight decrease in predicted *Dst* to values less than zero. Across the interface, the velocity increases from ~350 km/s to ~700 km/s. For the 3 days preceding and following the interface the velocity is steady at these values. The high-speed portion of the stream interaction region is accompanied by some southward B_z and velocities of ~750 km/s, so that values of $Dst < 0$ are predicted as well as observed.

The case shown in Figure 12 is also unlike that in Figures 10 and 11 in that the PVO overpredicts values of observed *Dst*. However, predictions of $Dst \approx 0$ for most of the time interval seem reasonable when the prevailing solar wind characteristics are examined. The distinguishing feature in this case is that the density at 0.7 AU is, on average, very high throughout this period (~35/cm³) as opposed to the overall database average of ~23/cm³. This density enhancement and lack of significant southward B_z represent an increase in magnetopause currents and absence of ring current energization, leading to predictions of $Dst > 0$. Since observations at 1 AU show that more negative *Dst*

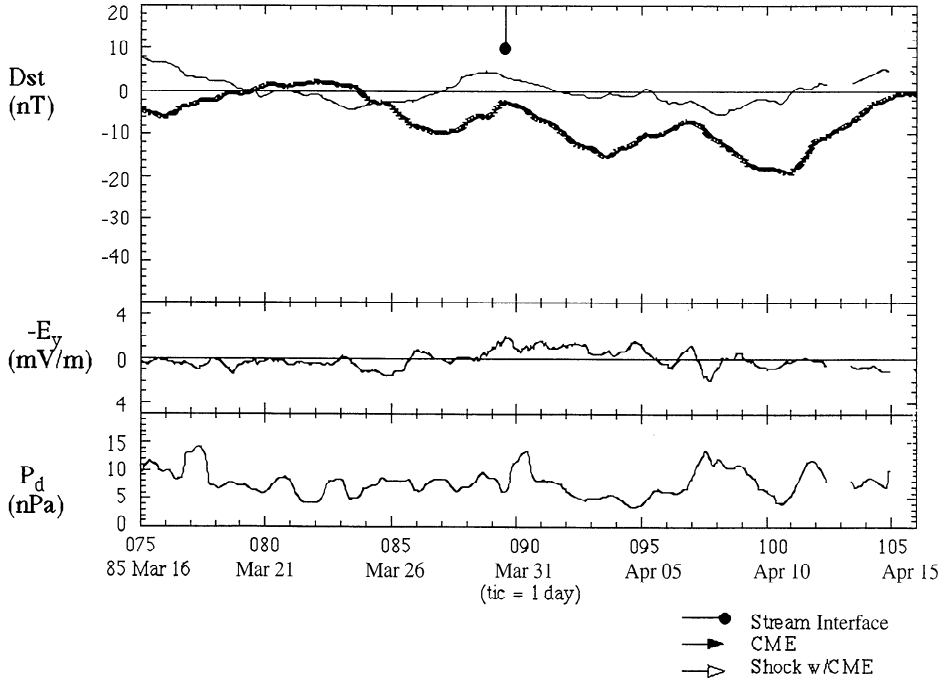

Figure 12. (Top) Comparison of predicted *Dst* from PVO data (thin line) and observed *Dst* from midlatitude ground stations (thick line) during March 15 through April 15, 1985. (Middle) Solar wind electric field. (Bottom) Dynamic pressure.

occurs, it may be concluded either that the characteristics of the solar wind changed between 0.7 AU and 1 AU or that different solar wind is reaching Earth and Venus throughout most of the period. Examination of the positions of PVO and Earth indicates that both PVO and Earth were in the same solar sector during this time period. Thus both locations should be seeing similar solar wind. The explanation of the inferred differences between the 0.7-AU and 1.0-AU values lies, perhaps, in the fact that the solar wind is dominated by small-scale fluctuations during this period, making it unlikely that observations will be correlated between two locations separated by such a large distance.

It is obvious from Figures 10, 11, and 12 that good *Dst* prediction capability is possible by using a solar wind monitor as far upstream of the Earth as 0.7 AU. The best agreement is obtained when PVO and the Earth are in near radial alignment with $\sim 0^{\circ}$ north/south separation. Also, the agreement between prediction and observations is much better during periods dominated by large-scale disturbances, such as CMEs and stream interaction regions, than those dominated by small-scale fluctuations. *Burton et al.* [1975] showed that the comparison between predicted *Dst* derived from Explorer 33 and 35 observations at 1.0 AU and actual *Dst* could be remarkably good. The various disagreements found here between the PVO-based predictions and 1.0-AU observations may be related to the evolution of the solar wind between 0.7 AU and 1.0 AU (e.g., the spatial and temporal changes of CMEs and stream interaction regions with increasing radial distance, and radial variations of B_z and ρ different from the r^{-1} and r^{-2} assumed here). Although it is not considered in this study, that evolution can in principle be modeled by using currently available MHD codes.

Conclusions

The present survey of the characteristics of stream interaction regions and coronal mass ejections allowed us to assess the potential geomagnetic effectiveness of each type of solar wind disturbance. It was found that both stream interaction regions and CMEs can have the high velocities and southward magnetic fields conducive to geomagnetic storm production. However, CMEs exhibit the strongest southward fields and highest velocities over longer time periods. Therefore CMEs are more likely to cause the largest geomagnetic storms. On the other hand, a small number of stream interaction regions also exhibit the VB_z characteristics associated with large geomagnetic storms. The existence of this population may explain the source of the major storms identified by *Gosling et al.* [1990] that were not associated with CMEs. From a survey of the characteristics of VB_z and ρV^2 both before and after stream interaction region passage, and before the CME leading edge and within the CME itself, it is found that the post-stream interface regions are more likely to be geomagnetically effective than the pre-stream interface regions. Pre-stream interface regions and quiet solar wind have similar characteristics and are not very likely to be geomagnetically effective. Both the pre-CME and post-CME regions have similar characteristics and are very likely to be a source of geomagnetic storms of all sizes.

These observed characteristics are consistent throughout all phases of the solar cycle. Thus during solar maximum, when CMEs are the most frequently observed solar wind disturbances, most geomagnetic storms, including the largest storms, will be produced by CMEs. During solar minimum, most geomagnetic storms will be produced by stream interaction regions, since stream interaction regions are the dominant solar wind disturbances during this period. However, even during solar minimum the largest storms will still be produced by CMEs.

The comparison of observed *Dst* and that predicted from observations at 0.7 AU shows that excellent predictions can be obtained from as far as ~ 0.3 AU upstream of the Earth. However, this capability is spatially and temporally dependent. The best predictions are made when the monitor is close to the ecliptic plane and there is near-radial alignment with the Earth-Sun line. Also, predictions are best for periods dominated by large-scale disturbances (i.e., CMEs) which are the source of the major geomagnetic storms. This capability can be further improved by incorporating a model for disturbance evolution into the *Dst* prediction algorithm of *Burton et al.* [1975]. As a whole, the present studies reinforce the idea that "space weather" forecasting can be improved by early detection of fast CMEs. The challenge in this case is to deal with the technological problem of maintaining an observational outpost far enough upstream.

Acknowledgements. The Editor thanks K. Takahashi and another referee for their assistance in evaluating this paper.

References

Akasofu, S. I., A source of the energy for geomagnetic storms and auroras, *Planet. Space Sci., 12*, 801-833, 1964.

Aubry, M. P., and R. L. McPherron, Magnetotail changes in relation to the solar wind magnetic field and magnetospheric substorms, *J. Geophys. Res.*, *76*, 4381-4401, 1971.

Aubry, M. P., C. T. Russell, and M. G. Kivelson, Inward motion of the magnetopause before a substorm, *J. Geophys. Res.*, *75*, 7018-7031, 1970.

Burlaga, L. F., K. W. Behannon, and L. W. Klein, Compound streams, magnetic clouds, and major geomagnetic storms, *J. Geophys. Res.*, *92*, 5725-5734, 1987.

Burton, R. K., R. L. McPherron, and C. T. Russell, An empirical relationship between interplanetary conditions and *Dst*, *J. Geophys. Res.*, *80*, 4204-4214, 1975.

Colin, L., The Pioneer Venus Program, *J. Geophys. Res.*, *85*, 7575-7598, 1980.

Dungey, J. W., Interplanetary magnetic field and the auroral zones, *Phys. Rev. Lett.*, *6*, 47-48, 1961.

Fairfield, D., and J. Cahill, Transition region magnetic field and polar magnetic disturbances, *J. Geophys. Res.*, *71*, 155-169, 1966.

Farrugia, C. J., M. P. Freeman, L. F. Burlaga, R. P. Lepping, and K. Takahashi, The Earth's magnetosphere under

continued forcing: Substorms activity during the passage of an interplanetary magnetic cloud, *J. Geophys. Res.*, *98*, 7657-7671, 1993.

Gosling, J. T., J. R. Ashbridge, S. J. Bame, and W. C. Feldman, Solar wind stream interfaces, *J. Geophys. Res.*, *83*, 1401-1411, 1978.

Gosling, J. T., D. N. Baker, S. J. Bame, W. C. Feldman, and R. D. Zwickl, Bidirectional solar wind electron heat flux events, *J. Geophys. Res.*, *92*, 8519-8535, 1987.

Gosling, J. T., S. J. Bame, D. J. McComas, and J. L. Phillips, Coronal mass ejections and large geomagnetic storms, *Geophys. Res. Lett.*, *17*, 901-904, 1990.

Gosling, J. T., D. J. McComas, J. L. Phillips, and S. J. Bame, Geomagnetic activity associated with Earth passage of interplanetary shock disturbances and coronal mass ejections, *J. Geophys. Res.*, *96*, 7831-7839, 1991.

Hirshberg, J., and D. S. Colburn, Interplanetary field and geomagnetic variations: A unified view, *Planet. Space Sci.*, *17*, 1183-1206, 1969.

Intriligator, D. S., J. H. Wolfe, and J. D. Mihalov, The Pioneer Venus Orbiter plasma analyzer experiment, *IEEE Trans. Geosci. Remote Sens.*, *GE-18*, 39-43, 1980.

Klein, L. W., and L. F. Burlaga, Interplanetary magnetic clouds at 1AU, *J. Geophys. Res.*, *87*, 613-624, 1982.

Lindsay, G. M., J. G. Luhmann, C. T. Russell, and P. R. Gazis, On the sources of interplanetary shocks at 0.72 AU, *J. Geophys. Res.*, *99*, 11-17, 1994.

Murayama, T., Coupling function between solar wind parameters and geomagnetic indices, *Rev. Geophys.*, *20*, 623-629, 1982.

Ogilvie, K. W., L. F. Burlaga, and T. D. Wilkerson, Plasma observations on Explorer 34, *J. Geophys. Res.*, *73*, 6809-6824, 1968.

Pizzo, V. J., The evolution of corotating stream fronts near the ecliptic plane in the inner solar system, 2, Three-dimensional tilted dipole fronts, *J. Geophys. Res.*, *96*, 5405-5420, 1991.

Russell, C. T., R. L. McPherron, and R. K. Burton, On the cause of geomagnetic storms, *J. Geophys. Res.*, *79*, 1105-1109, 1974.

Russell, C. T., R. C. Snare, J. D. Means, and R. C. Elphic, Pioneer-Venus Orbiter fluxgate magnetometer, *IEEE Trans. Geosci. Remote Sens.*, *GE-18*, 32-35, 1980.

Sawyer, C., and M. Haurwitz, Geomagnetic activity at the passage of high-speed streams, *J. Geophys. Res.*, *81*, 2435-2436, 1976.

Sheeley, N., and J. W. Harvey, Geomagnetic disturbances during 1978 and 1979, *Sol. Phys.*, *70*, 237-249, 1981.

Sheeley, N., J. W. Harvey, and W. C. Feldman, Coronal holes, solar wind streams, and recurrent geomagnetic disturbances: 1973-1976, *Sol. Phys.*, *49*, 271-278, 1976.

Siscoe, G. L., A unified treatment of magnetospheric dynamics with applications to magnetic storms, *Planet. Space Sci.*, *14*, 947-967, 1966.

Siscoe, G. L., V. Formisano, and A. J. Lazarus, A calibration of the magnetopause, *J. Geophys. Res.*, *73*, 4869-4874, 1968.

Tsurutani, B. T., B. E. Goldstein, E. J. Smith, W. D. Gonzales, Frances Tang, S. I. Akasofu, and R. R. Anderson, The interplanetary and solar causes of geomagnetic activity, *Planet. Space Sci.*, *38*, 109-126, 1990.

Tsurutani, B. T., W. D. Gonzales, F. Tang, and Y. T. Lee, Great magnetic storms, *Geophys. Res. Lett.*, *19*, 73-76, 1992.

G. M. Lindsay, J. G. Luhmann, and C. T. Russell, Institute of Geophysics and Planetary Physics, University of California, Los Angeles, 405 Hilgard Avenue, Los Angeles, CA 90024 (e-mail: gretchen@igpp.ucla.edu)

(Received July 25, 1994; revised January 26, 1995; accepted January 26, 1995.)